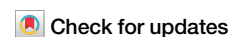Article

Dual-function FeCo bimetallic nanoclusters for ammonia electrosynthesis from nitrate/nitrite reduction

Check for updates

Miaosen Yang[1,2,6], Mingying Chen[3,6], Youqing Wang [4 ✉], Junjie Ma[3], Lang Zhang[3], Cejun Hu [4 ✉], Longchao Zhuo[5], Yanhong Feng[3] & Xijun Liu [3 ✉]

Ammonia (NH_3) plays a vital role in agriculture and chemical manufacturing, yet its conventional production is energy-intensive and environmentally harmful. Developing cleaner, more efficient alternatives is essential. Here we show a newly developed dual-metal nanocluster catalyst, $Fe_2Co_1/$NC, that effectively converts nitrate and nitrite pollutants into NH_3 through an electrochemical process. This catalyst achieves high NH_3 production rates and Faradaic efficiency, surpassing single-metal Fe/NC and Co/NC catalysts, and remains stable over extended use. When incorporated into nitrate- or nitrite-based zinc batteries, the system enables simultaneous NH_3 production and electricity generation, highlighting its potential for coupled energy recovery and environmental remediation. This work provides valuable design principles for bimetallic nanocluster catalysts and offers a promising strategy for the sustainable conversion of nitrogen-containing waste into useful chemicals.

Ammonia (NH_3) is a vital raw material in both agricultural and chemical production[1–3]. While the Haber-Bosch process currently dominates industrial production, its severe energy penalties (1–2% global energy consumption) and substantial CO_2 emissions fundamentally conflict with carbon neutrality objectives[4–6]. This contradiction has driven paradigm-shifting innovations in electrochemical NH_3 synthesis, particularly through nitrogen reduction (NRR) and nitrate/nitrite reduction (NO_3RR/NO_2RR) pathways[7,8]. Despite the theoretical potential of NRR to be green, the high stability of the N≡N triple bond (dissociation energy of 941 kJ mol^{-1}), coupled with the nonpolar nature of nitrogen and poor aqueous solubility, resulted in unsatisfactory NH_3 yields and Faraday efficiencies (FEs)[9,10]. In contrast, NO_3RR/NO_2RR powered by renewable energy, is a competitive and promising technology[11]. Principally, NO_3RR/NO_2RR is thermodynamically and kinetically superior to NRR[12]. Besides, this innovative approach utilizes NO_3^-/NO_2^-, abundant nitrogen sources in industrial wastewater, enabling direct conversion to NH_3 under ambient conditions[13]. This technology has the dual advantage of cleaning up nitrogen pollution, as well as producing high-purity NH_3[14]. Nevertheless, NO_3RR/NO_2RR produces a variety of by-products (e.g., N_2, NO_x) due to its complex reaction pathway, which affects selectivity and NH_3 yield[15]. Therefore, designing catalysts with superior activity and high selectivity is the critical key to achieving efficient NO_3RR/NO_2RR[16].

Nitrogen-doped carbon matrices exhibit prominent advantages in electrocatalysis, including their high electrical conductivity ensures rapid electron transfer. Concurrently, as catalyst supports, the enhanced surface hydrophilicity and the formation of metal-nitrogen coordination active sites ($M-N_x$) synergistically enhance the activity and stability of electrocatalytic reactions, making them ideal substrates for replacing noble metal catalysts[17–20]. Recently, non-noble single-atom catalysts (SACs) anchored on nitrogen-doped carbon matrices have attracted extensive attention in NO_3RR/NO_2RR studies[21–24], owing to their distinctive geometrical configurations, tunable electronic properties, and near-theoretical-limit atomic utilization efficiency[25]. Yet, non-noble single-metal active sites often suffer from low selectivity and insufficient stability[26]. To broaden the application of SACs, the researchers have developed

[1]School of Chemical Engineering, Northeast Electric Power University, Jilin, China. [2]Nanchang Institute of Technology, Nanchang, China. [3]MOE Key Laboratory of New Processing Technology for Nonferrous Metals and Materials, Guangxi Key Laboratory of Processing for Non-ferrous Metals and Featured Materials, School of Resources, Environment and Materials, Guangxi University, Nanning, Guangxi, China. [4]College of Materials Science and Engineering, Fuzhou University, Fuzhou, Fujian, China. [5]School of Materials Science and Engineering, Xi'an University of Technology, Xi'an, China. [6]These authors contributed equally: Miaosen Yang, Mingying Chen. ✉e-mail: 1316033097@qq.com; cejun_hu@fzu.edu.cn; xjliu@gxu.edu.cn

a variety of modulation methods for designing atomic sites, including replacing ligand atoms[27], structuring metal-organic frameworks[28,29], constructing ligand structures[30], and building bimetallic nanoclusters[31]. Among them, the strategy of constructing bimetallic nanoclusters has garnered significant attention, attributed to its dual advantages of the ultra-high atomic utilization efficiency of single atoms and synergistic catalysis[32,33]. An and his research team employed Cu-Ni bimetallic clusters in combination with constraint engineering for the first time to solve the problems of slow NO_3RR kinetics, severe shortage of catalytically active sites, and side reactions affecting the catalytic efficiency of monometallic catalysts[34]. Lee et al. achieved a high NH_3 yield (4.625 mmol h^{-1} cm^{-2}) for powdered NO_3RR catalysts by in-situ constructing CuCo bimetallic clusters and maximizing the synergistic effect of two metal[35]. However, reports on the design of bifunctional bimetallic cluster catalysts catering to both NO_3RR and NO_2RR remain scarce. Accordingly, the rational design of highly efficient multifunctional metal cluster catalysts has become a key research frontier in the contemporary landscape.

Herein, we report the Fe-Co bimetallic nanocluster catalysts (Fe_2Co_1/NC), which are anchored within a nitrogen-doped porous carbon (NC) matrix, exhibiting pronounced bifunctional activity for NO_3RR and NO_2RR. The Fe_2Co_1/NC architecture, engineered through hydrofluoric acid (HF) etching of a sacrificial silica template, yields a well-defined conductive carbon framework. This structural design not only facilitates efficient charge transfer kinetics and enhances overall electrical conductivity but also maximizes the exposed density of catalytically active sites. Furthermore, the porous carbon matrix serves as a high-surface-area scaffold for immobilizing Fe-Co nanoclusters, enabling synergistic enhancement of catalytic performance. Consequently, the Fe_2Co_1/NC catalyst demonstrates exceptional activity for NO_3RR and NO_2RR, with its performance metrics significantly outperforming those of single-metal counterparts (Fe/NC, Co/NC). Notably, $Zn-NO_3^-$ and $Zn-NO_2^-$ batteries equipped with Fe_2Co_1/NC cathodes achieve remarkable power densities while sustaining NH_3 production, highlighting their practical utility in energy conversion technologies and the valorization of nitrogenous waste.

Results and discussion
Synthesis and characterization of Fe_2Co_1/NC

Figure 1a illustrates the process flow for the preparation of Fe_2Co_1/NC catalyst loaded on NC using SiO_2 as a hard template, with the core steps including precursor impregnation, high-temperature carbonization, and template etching (see Synthesis Methods for details). To elucidate the morphological features of the catalyst, comprehensive characterizations including scanning electron microscopy (SEM), transmission electron microscopy (TEM), and X-ray diffraction (XRD) were performed. SEM images (Fig. 1b–f) reveal uniformly porous carbon architectures across all Fe: Co molar ratios (1:1, 1:2, 2:1, 1:4, 4:1), resulting from selective etching of SiO_2 templates by HF. This three-dimensional interconnected pore structure not only ensures high electrical conductivity but also significantly increases the exposure of electrochemically active sites, thereby optimizing charge transfer kinetics[36]. Further TEM characterization of Fe_2Co_1/NC corroborates its porous framework (Fig. 1g, h). Aberration-corrected high-angle annular dark-field scanning transmission electron microscopy (HAADF-STEM) image analysis directly visualizes that sub-nanometric Fe and Co metal nanoclusters with an average size of 0.90 nm are densely dispersed on the porous carbon matrix (Fig. 1i). This unique nanostructure
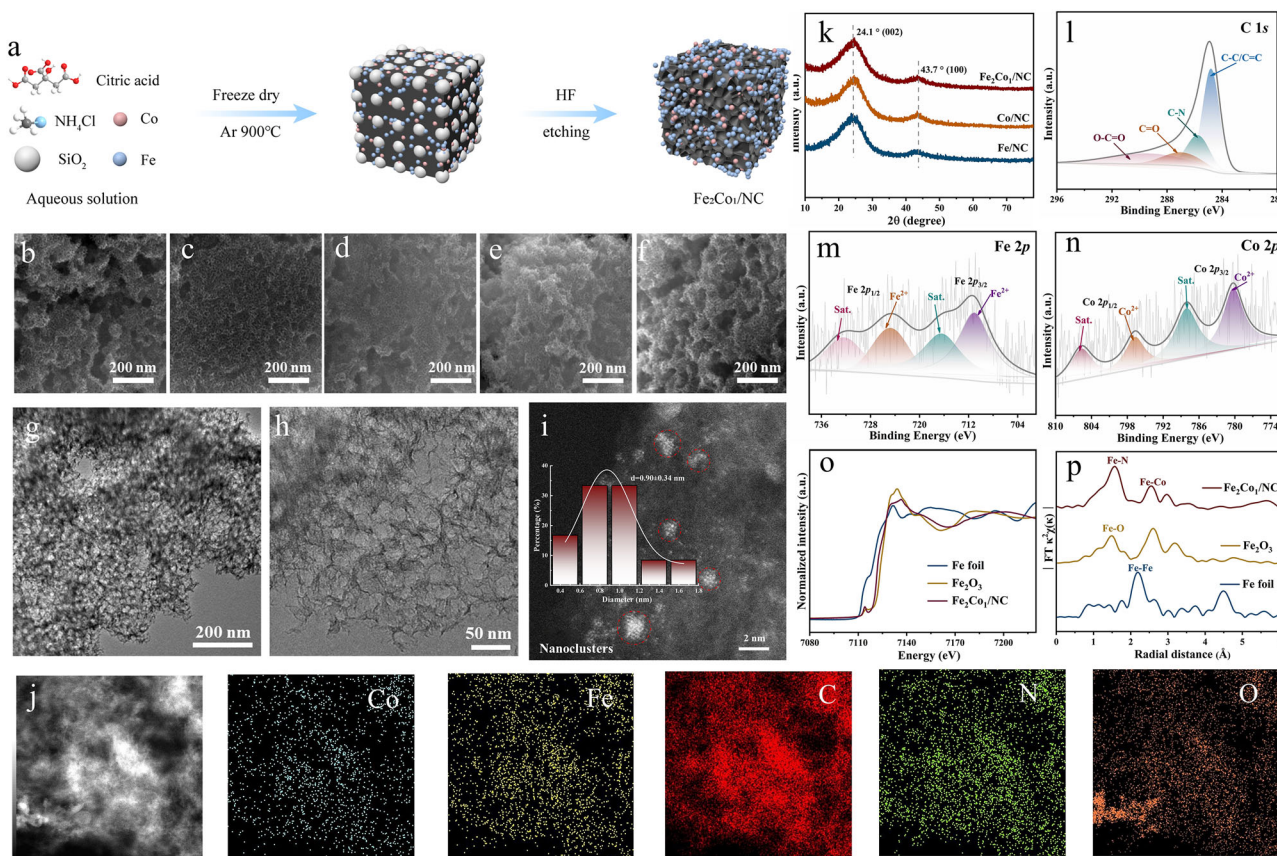

Fig. 1 | Synthesis and Characterization of catalysts. a Synthesis process of Fe_2Co_1/NC. SEM images of **b** Fe_1Co_1/NC, **c** Fe_1Co_2/NC, **d** Fe_2Co_1/NC, **e** Fe_1Co_4/NC, **f** Fe_4Co_1/NC. **g, h** TEM image and **i** Aberration-corrected HAADF-STEM image of Fe_2Co_1/NC, red circles highlight bimetallic nanoclusters (inset: the particle size distribution of FeCo sub-nanoclusters). **j** HAADF-STEM image and corresponding EDS elemental maps for Fe, Co, C, N, and O. **k** XRD patterns of Fe_2Co_1/NC, Fe/NC and Co/NC. XPS spectra of **l** C 1 s, **m** Fe 2p, **n** Co 2p for Fe_2Co_1/NC. **o** Fe K-edge XANES spectra of Fe_2Co_1/NC and the standard samples and **p** their corresponding FT-EXAFS spectra.

may facilitate interfacial electron transfer kinetics, offering a strategy to enhance electrocatalytic efficiency in complex multi-step reactions[37]. The Energy-dispersive X-ray spectroscopy (EDS) mapping manifests that Fe, Co, C, N, and O are well dispersed over carbon substrate (Fig. 1j). Furthermore, the XRD spectrum of Fig. 1k indicates broad diffraction peaks at about 24.1° and 43.7°, corresponding to the (002) and (100) crystal planes of graphitic carbon, respectively[38]. In contrast, the absence of diffraction peaks from the Fe/Co metal or alloy crystalline phases indicates that the metal species are present in the form of sub-crystalline clusters, in agreement with the TEM results. This may be due to the low content of Fe and Co elements in the samples and the small size of the nanoclusters formed[39].

Complementary to these analyses, the chemical composition and elemental valence states of Fe_2Co_1/NC were systematically characterized using X-ray photoelectron spectroscopy (XPS). XPS spectra confirm the presence of elements Fe, Co, C, N, and O in Fe_2Co_1/NC, which is in line with the EDS-mapping results (Fig. 1l–n and Figs. S1, 2). The C1s XPS spectra showed characteristic peaks at 289.84, 287.11, 285.82, and 284.80 eV, corresponding to O-C=O, C=O, C-N, and C-C/C=C bonds, respectively (Fig. 1l)[40]. The deconvoluted N1s spectrum (Fig. S1) exhibits five resolved components assigned to distinct nitrogen configurations: oxidized species (402.59 eV), graphitic N (401.33 eV), pyrrolic N (400.33 eV), pyridinic N (399.26 eV), and a characteristic metal-nitrogen (M-N) coordination peak at 398.36 eV[41]. The O 1 s analysis (Fig. S2) reveals oxygen-containing moieties including O-C=O (534.56 eV), C-O (532.89 eV), C=O (531.37 eV), alongside a definitive metal-oxygen (M-O) coordination signal at 530.09 eV. The concurrent presence of M-N and M-O bonds in Fe_2Co_1/NC confirms atomic-level coordination of Fe/Co centers with adjacent N and O ligands. Such interactions between the metal and N and O contribute to the high dispersibility of the metal nanoclusters, preventing their aggregation and growth during the reaction process[42]. The high-resolution Fe 2p XPS spectrum (Fig. 1m) exhibits characteristic spin-orbit doublets with Fe $2p_{3/2}$ and Fe $2p_{1/2}$ components at 711.1 eV and 724.7 eV, respectively, both diagnostic of divalent iron (Fe^{2+}). Shake-up satellite features at 716.4 eV and 732.5 eV further confirm octahedral coordination of Fe^{2+} with oxygen ligands[43]. The high-resolution Co 2p XPS spectrum (Fig. 1n) exhibits characteristic spin-orbit doublets with Co $2p_{3/2}$ and Co $2p_{1/2}$ components at 780.3 eV and 796.4 eV, respectively, both signatures of divalent cobalt (Co^{2+}). Additional shake-up satellite features are definitively assigned at 788.1 eV (associated with Co $2p_{3/2}$) and 805.5 eV (corresponding to Co $2p_{1/2}$)[44]. Critically, XPS analysis confirmed the absence of metallic iron (Fe^0) and cobalt (Co^0) species, consistent with phase identification derived from XRD characterization. X-ray absorption spectroscopy (XAS) was utilized to elucidate the electronic structure and local coordination environment of the as-synthesized sample. In the Fe K-edge X-ray absorption near-edge structure (XANES) spectra (Fig. 1o), the Fe XANES absorption edge for Fe_2Co_1/NC lies between those of Fe foil and Fe_2O_3, indicating that Fe is in a partially oxidized valence state. The k^2-weighted Fourier-transform extended X-ray absorption fine structure (FT-EXAFS) spectra (Fig. 1p) reveals a prominent peak at 1.57 Å for Fe_2Co_1/NC, attributed to Fe-N bonding, which aligns with the N 1 s XPS analysis. Notably, the FT-EXAFS spectra also exhibit a peak at 2.54 Å, corresponding to Fe-Co bonding, providing evidence of a direct interaction between Fe and Co[8]. The above analytical techniques collectively corroborate both the effective synthesis of the Fe_2Co_1/NC architecture and its inherent structural superiorities.

NO3RR performance evaluation

To evaluate the NO_3RR performance of the synthesized catalysts, a series of electrochemical measurements were conducted using a conventional three-electrode system in an H-battery configuration. Linear sweep voltammetry (LSV, Fig. 2a) tests in 0.1 M K_2SO_4 and 0.1 M KNO_3 electrolytes reveals that the Fe_2Co_1/NC catalyst exhibits a more rapid increase in current density with negative potential progression compared to Co/NC and Fe/NC counterparts, demonstrating superior catalytic activity for NO_3RR. Notably, Fe_2Co_1/NC achieves a significantly enhanced current density of $-81.79\,mA\,cm^{-2}$ at $-1.2\,V$ vs. RHE, indicating that the bimetallic

configuration effectively promotes NH_3 generation while suppressing the competing hydrogen evolution reaction (HER).

To identify the optimal catalyst, we systematically assessed the FEs and NH_3 production rate of Fe_xCo_y/NC catalysts across Fe:Co ratios (1:1, 1:2, 2:1, 1:4, 4:1), along with monometallic Fe/NC and Co/NC controls. FEs and production rates were calculated from chronoamperometric test (I-T) and NH_3 quantification (UV-Vis spectrophotometry of diluted post-electrolysis electrolyte, Fig. S3). As depicted in Fig. 2b, Fe_2Co_1/NC exhibits the highest FEs at all tested potentials, demonstrating superior selectivity for the NO_3RR. Notably, it achieves the highest FE at $-1.0\,V$ vs. RHE, confirming maximal NO_3^- to NH_3 conversion selectivity at Fe:Co = 2:1. Furthermore, the significantly higher FE of Fe_2Co_1/NC versus monometallic controls confirms a marked synergistic effect within Fe-Co nanoclusters for promoting NO_3RR, consistent with established literature[39]. As depicted in Fig. 2c, the Fe_2Co_1/NC catalyst exhibits optimal NO_3RR performance at $-1.0\,V$ vs. RHE under standard conditions, achieving a FE of 85.6% and a peak NH_3 production rate of 171.5 μmol h^{-1} cm^{-2}. A comparative analysis with recently reported catalysts (Table S1) reveals that the Fe_2Co_1/NC material exhibits significantly superior overall catalytic performance. Notably, the FE exhibits a systematic decline with positive potential shifts, decreasing considerably to 42.7% at $-1.2\,V$ vs. RHE. This behavior is attributable to the intensified HER, which competes with NO_3RR and diminishes catalyst selectivity towards the NH_3 synthesis pathway[45].

To further elucidate intrinsic activity differences, the electrochemical active surface area (ECSA) of each catalyst was evaluated via double-layer capacitance (C_{dl}) measurements within the non-faradaic potential region, while interfacial charge transfer kinetics were probed by electrochemical impedance spectroscopy (EIS). As shown in Figs. S4-S6 and Fig. 2d, the C_{dl} value of Fe_2Co_1/NC (34.0 mF cm^{-2}) significantly exceeds that of Fe/NC (11.1 mF cm^{-2}) and Co/NC (14.2 mF cm^{-2}), for different scanning rates from 50 mV s^{-1} to 100 mV s^{-1}. This indicates a larger ECSA for Fe_2Co_1/NC, implying greater exposure of electrochemically accessible active sites. Furthermore, EIS measurements conducted at $-1.0\,V$ vs. RHE (Fig. 2e) assessed the interfacial processes of Fe/NC, Co/NC, and Fe_2Co_1/NC. The Nyquist plots for all catalysts exhibit distinct high-frequency semicircular arcs, primarily corresponding to the charge transfer resistance (R_{ct}) at the electrode/electrolyte interface. Fe/NC displays the largest arc diameter, indicating the highest R_{ct}. In contrast, Fe_2Co_1/NC exhibits the smallest arc diameter, significantly lower than both Fe/NC and Co/NC, unequivocally confirming its minimal R_{ct}. This reduced R_{ct} directly reflects accelerated charge transfer kinetics at the Fe_2Co_1/NC interface during the NO_3RR. Integrating the C_{dl} and EIS analyses, the superior catalytic performance of Fe_2Co_1/NC, manifested in high FE and NH_3 production rate, is attributed to two key factors: (1) an enlarged ECSA providing abundant active sites, and (2) significantly reduced R_{ct} ensuring efficient interfacial electron transfer. This enhancement arises from the highly dispersed bimetallic (Fe-Co) nanoclusters within the porous NC matrix of Fe_2Co_1/NC. This structure maximizes active site exposure while optimizing electron conduction pathways, thereby synergistically promoting the overall kinetics of the NO_3RR.

Catalyst stability, a critical metric for practical implementation, was rigorously evaluated for Fe_2Co_1/NC. Cyclic electrolysis tests at $-1.0\,V$ vs. RHE over six cycles (Fig. 2f) demonstrate almost constant FEs and NH_3 production rates, indicating exceptional cycling stability. Furthermore, a 40-hour durability test (Fig. 2g) reveals stable current density without decay, confirming long-term operational robustness. After the catalytic reaction, the Fe_2Co_1/NC catalyst maintains its original porous morphology (Fig. S7), with no noticeable structural changes observed. Additionally, a comparison of the pre- and post-reaction XPS spectra (Fig. S8) shows no significant differences. These findings collectively demonstrate the excellent electrochemical stability of Fe_2Co_1/NC for NO_3RR. Additionally, to rigorously assess the catalyst's resilience in the presence of industrial wastewater contaminants, 0.01 M Cl^- was introduced into the electrolyte to simulate complex real-world matrices. As shown in Fig. S9, the NH_3 yield rate and FEs exhibits negligible changes across the applied potentials compared to
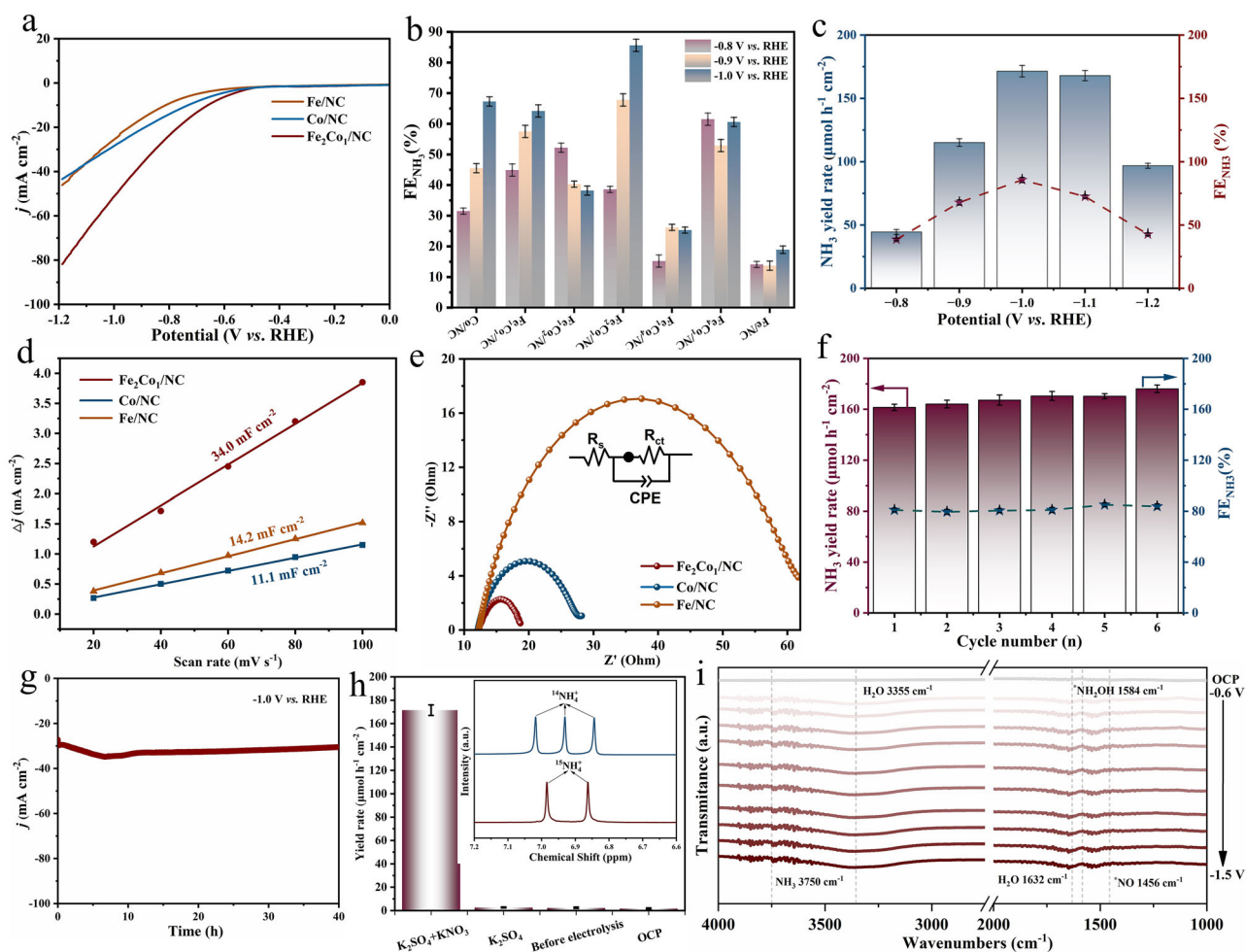
Fig. 2 | Electrocatalytic NO$_3$RR assessment. a The LSV curves for Fe$_2$Co$_1$/NC, Fe/NC and Co/NC. **b** Comparative FEs and NH$_3$ production rate of Fe$_x$Co$_y$/NC, Fe/NC and Co/NC at different potentials. **c** Potential-dependent FEs and NH$_3$ yield for Fe$_2$Co$_1$/NC. **d** ECSA measurements. (**e**) Nyquist plots from EIS. **f, g** Durability testing results. **h** Comparison of NH$_3$ generation rates under different conditions (inset: ^{1}H NMR spectra). **i** In situ FTIR spectroscopy of Fe$_2$Co$_1$/NC.

those in the original electrolyte. This consistent performance under chloride-rich conditions demonstrates the catalyst's excellent Cl$^-$ tolerance, underscoring its potential for practical application in nitrate-contaminated wastewater treatment systems.

To definitively confirm the origin of NH$_3$ and exclude potential contributions from environmental contamination or impurities, systematic control experiments were conducted (Fig. 2h). The analysis reveals negligible NH$_3$ detection under three conditions: at the OCP, in the absence of NO$_3^-$, and without electrochemical pretreatment. The observed NH$_3$ levels are substantially lower than the production rate (171.5 μmol h^{-1} cm^{-2}) achieved with Fe$_2$Co$_1$/NC under optimal NO$_3$RR conditions. Additionally, ^{15}N isotopic labeling was employed to definitively trace the nitrogen source of the electrogenerated NH$_3$ (inset in Fig. 2h). ^{1}H nuclear magnetic resonance (^{1}H NMR) analysis reveals a characteristic triplet for NH$_4^+$ when ^{14}NO$_3^-$ serves as the nitrogen source, whereas a distinct doublet is exclusively observed when ^{15}NO$_3^-$ is fed. These results conclusively demonstrate that the produced NH$_3$ originates directly from the NO$_3$RR, rather than from atmospheric N$_2$ fixation or external nitrogen contaminants[39].

To mechanistically elucidate the dynamic mechanism of the NO$_3$RR over Fe$_2$Co$_1$/NC catalysts, in situ Fourier-transform infrared spectroscopy (FTIR) was employed to track potential-dependent intermediates (Fig. 2i). Distinct spectral features emerged under cathodic polarization ($-0.6 \sim -1.5$ V vs. RHE), contrasting with negligible signals at OCP. The ν(O-H) and δ(H-O-H) absorption peaks at 3355 cm^{-1} and 1632 cm^{-1} indicate that the interfacial hydrolysis process continues to provide protons for the reaction, which is a key prerequisite for the proton-coupled electron

transfer (PCET) pathway[46]. the characteristic peaks of ν(NO) characteristic peak at 1456 cm^{-1} reveals the generation of nitric oxide (NO (ads)) in the adsorbed state, corroborating the activation of nitrate via the successive deoxygenation pathway (NO$_3^- \rightarrow$ NO$_2^- \rightarrow$ NO (ads)). The δ(NOH) absorption peaks at 1520 cm^{-1} are also observed during this process. δ(N-H) vibrational mode at 1584 cm^{-1} provides direct evidence for the presence of hydroxylamine (NH$_2$OH) intermediates[47], while the enhanced ν(N-H) vibration at 3750 cm^{-1} is a clear indication of the eventual generation of free NH$_3$[48]. The above in situ FTIR constructed a complete reaction pathway: NO$_3^- \rightarrow$ NO (ads)$\rightarrow$NOH $\rightarrow$ NH$_2$OH $\rightarrow$ NH$_3$.

To elucidate the role of the Fe$_2$Co$_1$/NC catalyst in enhancing the NO$_3$RR while suppressing the competing HER, density functional theory (DFT) calculations were performed. Given that the adsorption of NO$_3^-$ and H* is regarded as a prerequisite for catalytic activity[9,49], the d-band centers of three catalysts (Fe$_2$Co$_1$/NC, Fe/NC, and Co/NC) were first evaluated via projected density of states (PDOS) analysis (Fig. 3a). The results show that the d—band center of Fe/NC ($\varepsilon_d = -1.07$ eV) is higher than that of Co/NC ($\varepsilon_d = -1.37$ eV). Meanwhile, due to the interaction between Fe and Co atoms, the ε_d value of Fe$_2$Co$_1$/NC is adjusted to a moderate level of -1.12 eV, which effectively modulates the interaction between the metal active sites and reaction intermediates[50]. Subsequently, the adsorption energies (ΔE_{ad}) of NO$_3^-$ and H* on the catalysts were calculated. Notably, Fe$_2$Co$_1$/NC exhibits a higher ΔE_{ad} for NO$_3^-$ and a lower ΔE_{ad} for H* compared to Fe/NC and Co/NC (Fig. 3b). These results suggest that the bimetallic sites more readily capture NO$_3^-$, initiating the reduction reaction. Fe$_2$Co$_1$/NC demonstrates more favorable kinetic properties for the NO$_3$RR,
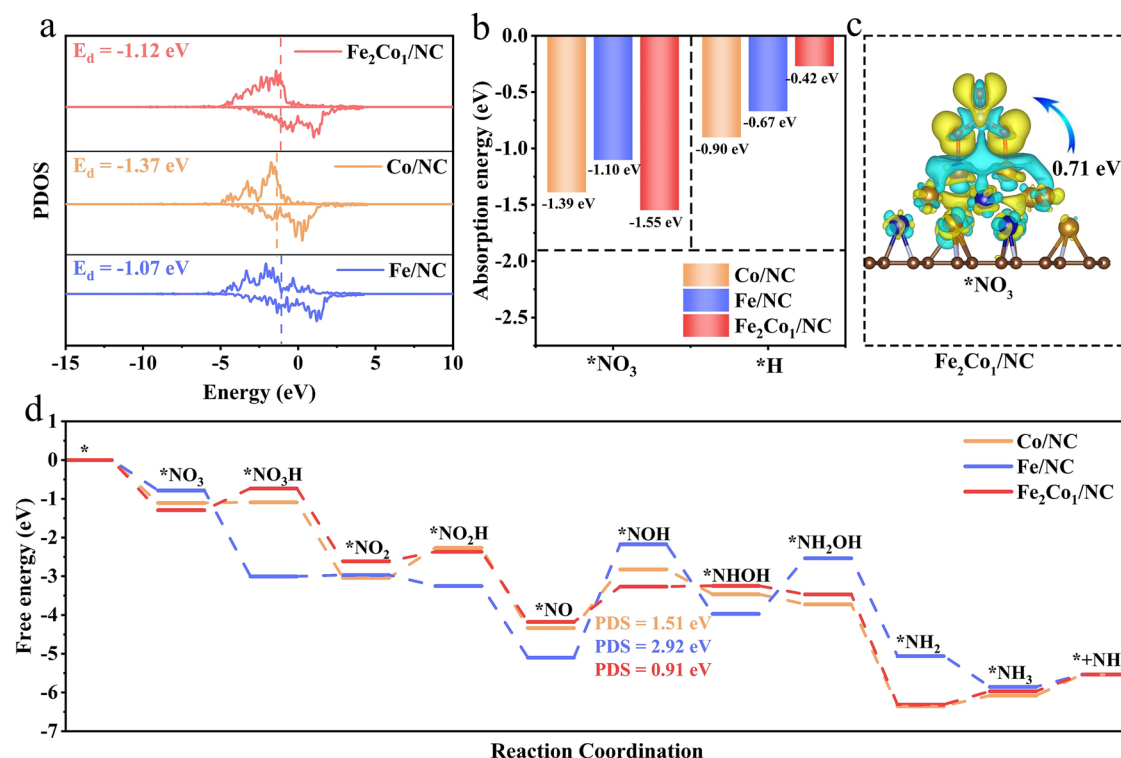
Fig. 3 | Theoretical calculation. a The PDOS and **b** Comparison of adsorption energies of reaction intermediates for Fe_2Co_1/NC, Fe/NC, and Co/NC. **c** Charge density differences of NO_3^- on Fe_2Co_1/NC. **d** The Gibbs free energy diagrams for NO_3RR.

while the weaker proton adsorption effectively suppresses the HER[51]. The preferential adsorption of NO_3^- over H^+ further confirms the selective promotion of NO_3RR and inhibition of HER on Fe_2Co_1/NC[52]. In addition, charge density difference analysis revealed significant electron transfer between the Fe_2Co_1/NC surface and the adsorbed NO_3^- (Fig. 3c), indicating efficient activation of NO_3^-, which is essential for subsequent reduction steps[53].

To further understand the reaction mechanism, the free energy profiles for the complete NO_3RR pathway were computed for each catalyst. As depicted in Fig. 3d, the potential-determining step (PDS) for the catalysts corresponds to the proton-electron transfer of *NO to *NOH (*NO + H^+ + e^- → *NOH). After *NOH is generated, the reaction proceeds further, ultimately producing NH_3 on the Fe_2Co_1/NC surface. Notably, the PDS energy barrier of Fe_2Co_1/NC (0.91 eV) is significantly lower than those of Co/NC (1.51 eV) and Fe/NC (2.92 eV), suggesting that bimetallic synergy effectively reduces the critical energy barrier, accelerates the conversion of NO_3^- to NH_3, and thereby enhances catalytic efficiency[50]. Collectively, both theoretical and experimental results validate that that the bimetallic Fe_2Co_1/NC catalyst not only promotes NO_3^- adsorption but also facilitates a more efficient reaction pathway by reducing energy barriers, thereby significantly enhancing NO_3RR performance.

Zn-NO_3^- battery performance evaluation

Based on the excellent structural chemistry and catalytic properties of Fe_2Co_1/NC, a Zn-NO_3^- battery system was successfully constructed using it as the cathode and Zn foil as the anode (Fig. 4a). To evaluate the electrochemical performance of Zn-NO_3^- batteries with different materials (Fe_2Co_1/NC, Fe/NC, and Co/NC) as cathode materials, the discharge performance tests were carried out in a mixed electrolyte of 0.1 M KNO_3 and 0.1 M K_2SO_4 (Fig. 4b). The results show that the battery based on Fe_2Co_1/NC cathode exhibits significantly better electrochemical performance with a peak power density as high as 0.39 mW cm^{-2} compared to Fe/NC and Co/NC batteries. In addition, the OCP of the battery is measured to be 0.71 V (Fig. 4c). To comprehensively evaluate the performance of the system, the

electrolyte after electrolysis was analyzed by UV-Vis absorption spectroscopy at different current densities (Fig. S10), from which the NH_3 yield of the Zn-NO_3^- battery based on the Fe_2Co_1/NC cathode and its FE is quantitatively determined. As shown in Fig. 4d, both the NH_3 yield and FEs increase simultaneously with the increase of current density. The optimal performance is achieved at a current density of 10 mA cm^{-2} with an NH_3 yield of 25.1 μmol h^{-1} cm^{-2} and a FE of 53.9%. The rate performance of the Zn-NO_3^- battery featuring a Fe_2Co_1/NC cathode was evaluated (Fig. 4e). An increase in current density from 2 mA cm^{-2} to 10 mA cm^{-2} results in a progressive widening of the gap between its charge and discharge curves. This characteristic response highlights the system's robust electrochemical behavior across different current densities.

Battery stability is a key indicator for evaluating its overall performance. As shown in Fig. 4f, the Zn-NO_3^- battery was subjected to a constant current discharge test for 15 h at a constant current density of 5 mA cm^{-2}. The results show that the Zn-NO_3^- battery with Fe_2Co_1/NC cathode exhibits a stable discharge voltage plateau, which fully confirms its excellent cycling stability. In conclusion, the bimetallic cluster architecture demonstrates not only high catalytic efficiency for NO_3^- to NH_3, but also exhibits high energy conversion efficiency and significant potential for practical engineering applications.

NO₂RR performance research

Nitrite anion (NO_2^-) presents unique advantages as a promising substrate for aqueous electrochemical NH_3 synthesis, including low N=O bond dissociation energy, favorable aqueous solubility, and relatively high redox potential. To evaluate the NO_2RR performance, the electrocatalytic performance of three synthesized catalysts (Fe_2Co_1/NC, Fe/NC, and Co/NC) for NO_2^- to NH_3 conversion was systematically evaluated through LSV measurements. As depicted in Fig. 5a, the LSV curves measured in 0.1 M KNO_2 and 0.1 M K_2SO_4 electrolyte reveal that the current density of Fe_2Co_1/NC is significantly higher than that of Fe/NC and Co/NC in the potential range of 0.0 V vs. RHE to −1.2 V vs. RHE, peaking at 150 mA cm^{-2}. This exceptional activity confirms the superior NO_2RR capability of Fe_2Co_1/NC,
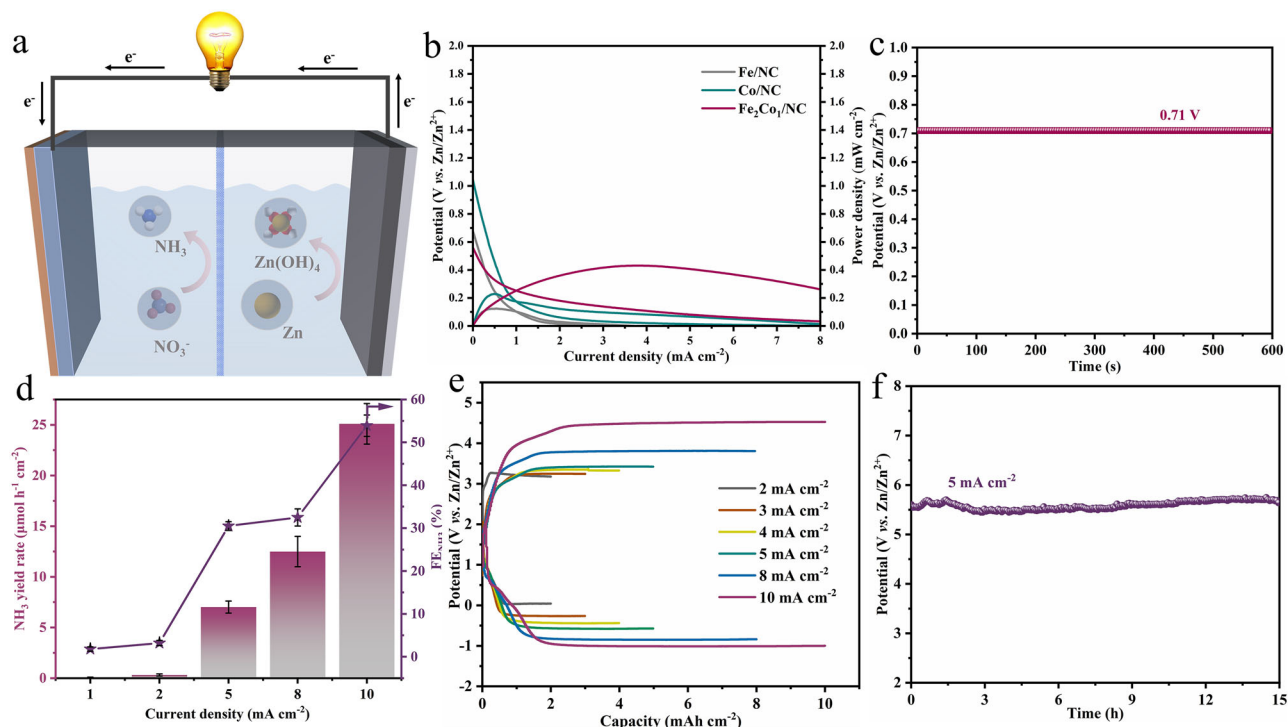
Fig. 4 | Performance evaluation of the Zn-NO$_3^-$ battery. a Schematic diagram of the battery configuration. **b** Discharge profiles. **c** OCP, **d** NH$_3$ yields and FEs at different current densities, **e** Charge and discharge curves at varying current densities, **f** Stability testing of the Zn-NO$_3^-$ battery based on Fe$_2$Co$_1$/NC as a cathode battery.

which establishes favorable kinetics for NH$_3$ synthesis. These results demonstrate that bimetallic cluster structures effectively synergize to enhance the intrinsic electrocatalytic activity of catalytic sites[54,55]. To identify optimal NO$_2$RR catalysts, we systematically evaluated the ammonia synthesis performance of Fe$_2$Co$_1$/NC, Fe/NC, and Co/NC within the potential window of −0.9 to −1.1 V *vs.* RHE. As depicted in Fig. 5b, NH$_3$ yield exhibits a positive potential dependence, with Fe$_2$Co$_1$/NC demonstrating superior NH$_3$ production rates that underscore its exceptional catalytic efficacy. This enhancement is attributed to bimetallic cluster-mediated synergistic effects, aligning with prior studies confirming the critical role of dual-metal configurations in NO$_2$RR pathways[3,56]. To precisely quantify FEs and NH$_3$ yield for Fe$_2$Co$_1$/NC catalysts, the I-T method (Fig. S11) coupled with UV-Vis spectroscopy (Fig. S12) was employed for systematic assessment. As depicted in Fig. 5c, the Fe$_2$Co$_1$/NC catalyst exhibits a peak NH$_3$ generation rate of 322.6 μmol h^{-1} cm^{-2} at a potential of −1.2 V *vs.* RHE, surpassing recently reported catalysts and highlighting the synergistic effect of bimetallic nanoclusters (Table S2). Its FEs show a typical volcano distribution, reaching an optimum value of 78.1% at −1.0 V *vs.* RHE, and then falling back to 63.4% at −1.2 V *vs.* RHE. This efficiency decay was attributed to the intensification of the HER at high cathodic potentials, which competes with the nitrite reduction process and thus inhibits the selectivity of NH$_3$ synthesis[57]. A long-term stability assessment of the Fe$_2$Co$_1$/NC catalyst was subsequently conducted (Fig. 5d). At a potential of −1.2 V *vs.* RHE, the catalyst maintains a stable current density of 40 mA cm^{-2} for 25 hours. This performance underscores the excellent catalytic stability of the Fe$_2$Co$_1$/NC catalyst over an extended period.

Zn-NO$_2^-$ battery performance evaluation

Building upon the excellent NO$_2$RR performance of the catalysts, researchers assembled Zn-NO$_2^-$ batteries using Fe$_2$Co$_1$/NC, Fe/NC, and Co/NC catalysts to investigate their electrochemical performance within a battery configuration systematically. Discharge tests were performed in a mixed electrolyte containing 0.1 M KNO$_2$ and 0.1 M K$_2$SO$_4$ (Fig. 6a). The results demonstrate that the Fe$_2$Co$_1$/NC-based battery exhibits significantly superior power density compared to those with single-metal Fe/NC or Co/

NC catalysts, peaking at approximately 4.58 mW cm^{-2} at 4.75 V *vs.* Zn/Zn^{2+}. Furthermore, the OCP of the Fe$_2$Co$_1$/NC-based Zn-NO$_2^-$ battery was measured at 1.43 V *vs.* Zn/Zn^{2+} (Fig. 6b). Furthermore, the stability of the Zn-NO$_2^-$ battery employing an Fe$_2$Co$_1$/NC cathode was evaluated (Fig. 6c). The battery demonstrates no significant performance degradation during continuous operation for 7 h across current densities ranging from 0.2 to 5 mA cm^{-2}.

To systematically assess the performance of the Zn-NO$_2^-$ battery with the Fe$_2$Co$_1$/NC cathode, the NH$_3$ yields and FEs were further measured at various current densities (Fig. 6d). The data reveal that the NH$_3$ yield reaches a peak value of 30.9 μmol·h^{-1} at 8 mA cm^{-2}, while the FE achieves 76.0% at 4 mA cm^{-2}. Subsequent charge-discharge tests (Fig. 6e) indicate that the voltage gap of the Zn-NO$_2^-$ battery systematically increased as the current density was stepped up from 0.5 mA cm^{-2} to 3.0 mA cm^{-2}. At a low current density of 0.5 mA cm^{-2}, the voltage gap was 1.49 V, while at a high current density of 3.0 mA cm^{-2}, the voltage gap widened to 2.19 V, indicating the excellent charging and discharging performance of the battery. Long-term cycling stability tests (Fig. 6f) confirm highly stable performance output over 24 h of continuous operation. Collectively, these electrochemical performance metrics demonstrate the significant potential of the Fe$_2$Co$_1$/NC material for NH$_3$ production in Zn-NO$_2^-$ battery. This system enables the dual-functional objective of synchronous ammonia synthesis and pollutant removal, offering a viable approach for the integration of electrocatalytic ammonia production and environmental remediation.

Conclusions

In this study, a bifunctional Fe$_2$Co$_1$/NC electrocatalyst was successfully synthesized via hydrogen fluoride etching of silica templates to construct porous carbon substrates, synergistically anchoring FeCo bimetallic nanoclusters as active sites. The catalyst exhibits excellent activity for NO$_3$RR and NO$_2$RR. Comprehensive structural characterizations including SEM, TEM, HAADF-STEM, XPS and XAFS collectively confirm the structural integrity of the material. In situ spectroscopy and theoretical simulations further elucidate the catalytic mechanism and reaction pathways. Electrochemical measurements demonstrate that Fe$_2$Co$_1$/NC
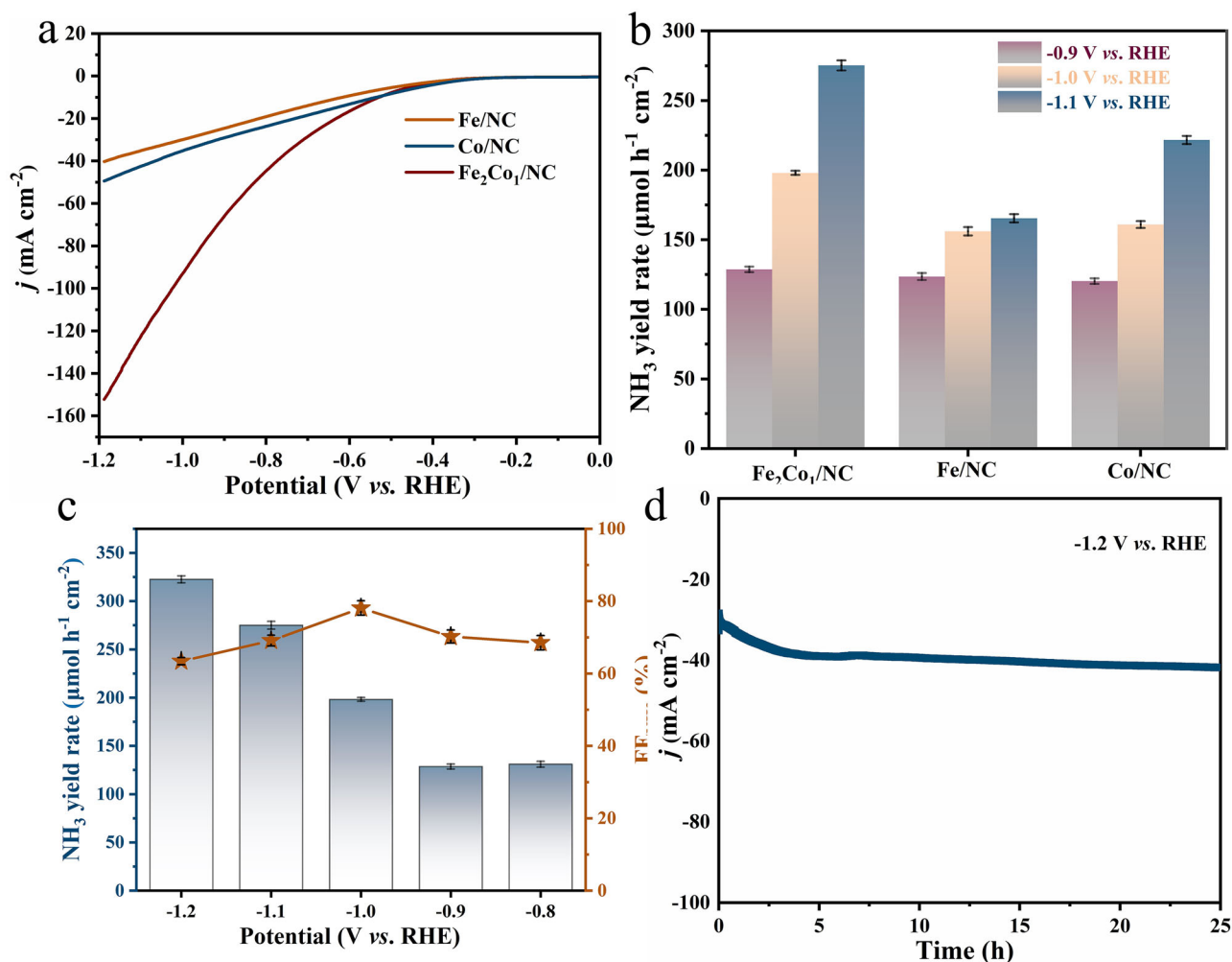
Fig. 5 | Electrocatalytic NO₂RR assessment. a The LSV curves for Fe_2Co_1/NC, Fe/NC and Co/NC. **b** FE and NH_3 production rate versus potential for Fe_2Co_1/NC, Fe/NC, and Co/NC. **c** Potential-dependent FEs and NH_3 yield for Fe_2Co_1/NC. **d** Long-term operational stability of Fe_2Co_1/NC.

achieves optimal NO_3^- to NH_3 conversion at -1.0 V *vs.* RHE, delivering an exceptional NH_3 yield of 171.5 µmol h^{-1} cm^{-2} and a FE of 85.6%. The catalyst maintains excellent operational stability for 40 h. When integrated into a Zn-NO$_3^-$ battery, the system simultaneously generates electricity (0.39 mW cm^{-2}), and NH_3 (25.1 µmol h^{-1} cm^{-2}, 53.9% FE). For NO₂RR, Fe_2Co_1/NC attains a peak FE of 78.1% at -1.0 V *vs.* RHE. The maximum NH_3 yield reaches 322.6 µmol h^{-1} cm^{-2} at -1.2 V *vs.* RHE, with sustained stability exceeding 25 hours. Assembled Zn-NO$_2^-$ battery exhibits substantially enhanced performance, attaining a power density of 4.58 mW cm^{-2}. Overall, this work offers a robust platform for dual-function nitrogen conversion and provides valuable guidance for designing high-performance bimetallic nanocluster catalysts.

Methods
Material synthesis
Synthesis of Fe_2Co_1/NC catalysts. Initially, citric acid monohydrate ($C_6H_8O_7 \cdot H_2O$, 5.0 g), ammonium chloride (NH_4Cl, 5.0 g), silica template (SiO_2, 1.5 g), iron(III) nitrate nonahydrate ($Fe(NO_3)_3 \cdot 9H_2O$, 0.33 g), and cobalt(II) nitrate hexahydrate ($Co(NO_3)_2 \cdot 6H_2O$, 0.12 g) were co-dissolved in 15 mL of deionized water. A homogeneous precursor solution was formed through ultrasonication-assisted magnetic stirring. This solution was subjected to vacuum freeze-drying to obtain a solid mixture, which was then thoroughly ground to yield a white precursor powder. Subsequently, the powder was subjected to high-temperature pyrolysis in a tube furnace under a continuous flow of high-purity argon (Ar). The thermal program was set to heat to the target carbonization

temperature of 900 °C at a ramping rate of 10 °C min^{-1}, followed by isothermal carbonization for 3 h. After natural cooling to room temperature, a black intermediate product was obtained. To remove the SiO_2 template, the product was immersed in a 5 wt% hydrofluoric acid (HF) aqueous solution and etched at room temperature for 10 h. Following etching, the sample was repeatedly washed with copious amounts of deionized water until a neutral pH was achieved to eliminate residual acid and dissolved silicon species. Finally, the washed solid product was dried in an oven at 60 °C, thus obtaining the target Fe_2Co_1/NC catalyst powder.

Synthesis of Fe_xCo_y/NC ($x{:}y$ = 4:1, 1:2, 1:1, 1:4). Synthesized using identical procedures but with adjusted Fe/Co precursor masses. Fe_xCo_y/NC ($x{:}y$ = 4:1, 1:2, 1:1, 1:4) were synthesized in the same steps, but the masses of Fe and Co were replaced with 0.4 g $Fe(NO_3)_3 \cdot 9H_2O$ and 0.072 g $Co(NO_3)_2 \cdot 6H_2O$ (4:1), 0.1667 g $Fe(NO_3)_3 \cdot 9H_2O$ and 0.2401 g $Co(NO_3)_2 \cdot 6H_2O$ (1:2), 0.25 g $Fe(NO_3)_3 \cdot 9H_2O$ and 0.1801 g $Co(NO_3)_2 \cdot 6H_2O$ (1:1), 0.1 g $Fe(NO_3)_3 \cdot 9H_2O$ and 0.2881 g $Co(NO_3)_2 \cdot 6H_2O$ (1:4). Fe_xCo_y/NC means that the total mass of the iron-containing material, 0.5 g, is used to determine the amount of substance n. The mass of the iron-containing material is found by substituting n of $X/X + Y$, and the mass of the cobalt-containing material is found by substituting n of $Y/X + Y$ for the mass of the cobalt-containing material.

Synthesis of Fe/NC. The procedure for the synthesis of Fe/NC is similar to that of Fe_2Co_1/NC. However, only 0.5 g of $Fe(NO_3)_3 \cdot 9H_2O$ was used as the sole metal precursor.
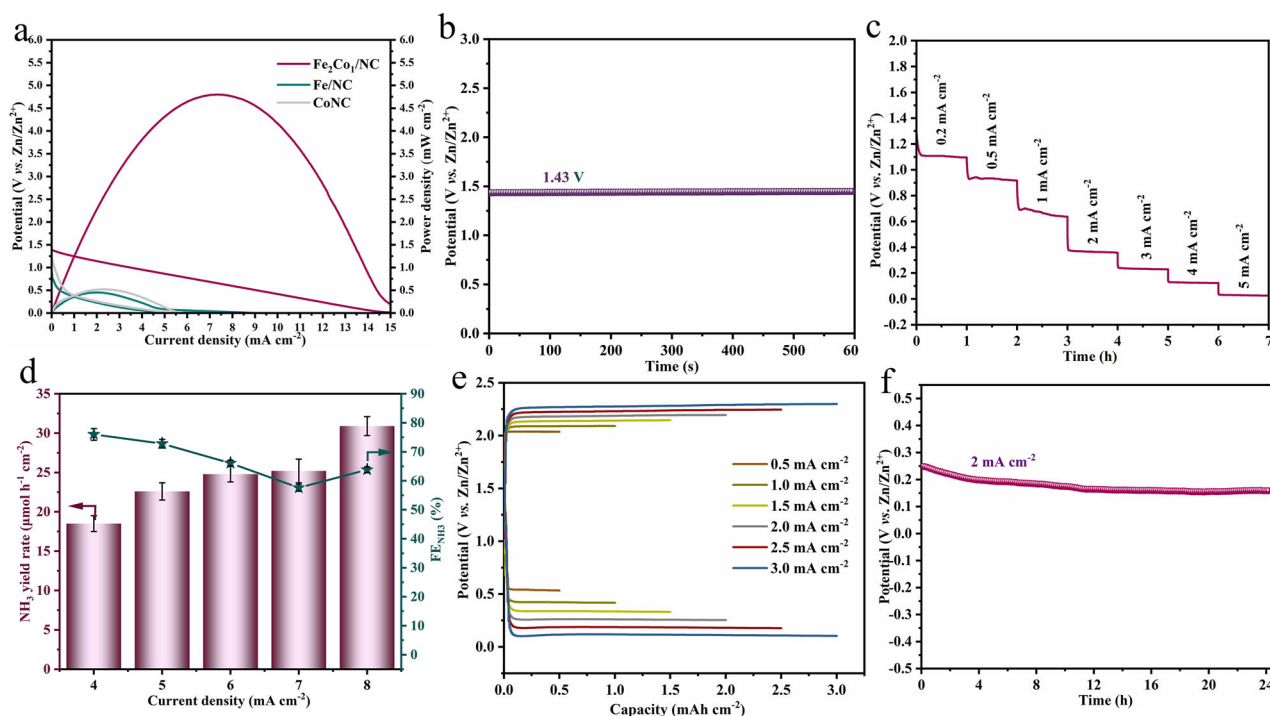
Fig. 6 | Characterization of the Zn-NO$_2^-$ battery. a Discharge curves. **b** OCP, **c** Discharge performance across current densities, **d** NH$_3$ yields and FEs versus current density, **e** Charge and discharge response at different current densities, and **f** Stability evaluation of the Zn-NO$_2^-$ battery based on Fe$_2$Co$_1$/NC as a cathode battery.

Synthesis of Co/NC. Co/NC was synthesized in the same steps as Fe$_2$Co$_1$/NC. However, only 0.5 g of Co(NO$_3$)$_2$·6H$_2$O was used as the sole metal precursor.

Data availability

The data supporting the findings of this study are included in the paper on the Supplementary Information and are also available upon request from the corresponding author. All NMR spectra recorded during this study are included in the Supplementary Data 1 file. The raw data for the theoretical calculations during this study are included in Supplementary Data 2 file. All the raw data for the figures during this study are included in Supplementary Data 3 file.

References

1. Sun, S. et al. Spin-related Cu-Co pair to increase electrochemical ammonia generation on high-entropy oxides. *Nat. Commun.* **15**, 260 (2024).
2. Shen, Z. et al. Highly accessible electrocatalyst with in situ formed copper-cluster active sites for enhanced nitrate-to-ammonia conversion. *ACS Nano* **19**, 4611–4621 (2025).
3. Liu, X. et al. Advances in the synthesis strategies of carbon-based single-atom catalysts and their electrochemical applications. *China Powder Sci. Technol.* **30**, 35–45 (2024).
4. An, T.-Y. et al. Utilizing the Wadsley-Roth structures in TiNb$_2$O$_7$@C microspheres for efficient electrochemical nitrogen reduction at ambient conditions. *Adv. Compos. Hybrid. Mater.* **7**, 201 (2024).
5. Dong, J.-H. et al. Engineering Ce promoter to regulate H* species to boost tandem electrocatalytic nitrate reduction for ammonia synthesis. *Adv. Funct. Mater.* **35**, 2422025 (2025).
6. Chen, M. et al. Advanced characterization enables a new era of efficient carbon dots electrocatalytic reduction. *Coord. Chem. Rev.* **535**, 216612 (2025).
7. Jiang, Z. et al. Molecular electrocatalysts for rapid and selective reduction of nitrogenous waste to ammonia. *Energy Environ. Sci.* **16**, 2239–2246 (2023).
8. Lu, H. et al. Electron-deficient asymmetric Co centers marry oxygen vacancy for NO$_3$RR: Excellent activity and anion resistance property. *Chem. Eng. J.* **503**, 158536 (2025).
9. Huang, Z. et al. Recent progress in electrocatalytic nitrogen reduction to ammonia (NRR). *Coord. Chem. Rev.* **478**, 214981 (2023).
10. Wu, T., Melander, M. M. & Honkala, K. Coadsorption of NRR and HER intermediates determines the performance of Ru-N4 toward electrocatalytic N$_2$ reduction. *ACS Catal.* **12**, 2505–2512 (2022).
11. Xiang, J. et al. Tandem electrocatalytic reduction of nitrite to ammonia on rhodium–copper single atom alloys. *Adv. Funct. Mater.* **34**, 2401941 (2024).
12. Choi, J. et al. Identification and elimination of false positives in electrochemical nitrogen reduction studies. *Nat. Commun.* **11**, 5546 (2020).
13. Ren, Z., Shi, K. & Feng, X. Elucidating the intrinsic activity and selectivity of Cu for nitrate electroreduction. *ACS Energy Lett.* **8**, 3658–3665 (2023).
14. Zhang, C. et al. Self-powered energy-efficient electrochemical nitrite reduction coupled with sulfion oxidation for ammonia synthesis and sulfur recovery over hierarchical cobalt sulfide nanostructures. *Appl. Catal. B Environ. Energy* **365**, 124991 (2025).
15. Cui, Z. et al. Multi-dimensional Ni@TiN/CNT heterostructure with tandem catalysis for efficient electrochemical nitrite reduction to ammonia. *Angew. Chem. Int. Ed.* **64**, e202501578 (2025).
16. He, N. et al. Efficient nitrate to ammonia conversion on bifunctional IrCu$_4$ alloy nanoparticles. *ACS Nano* **19**, 4684–4693 (2025).
17. Lian, K. et al. Coupling value-added methanol oxidation with CO$_2$ electrolysis by low-coordinated atomic Ni sites. *ACS Nano* **19**, 20001–20011 (2025).
18. Chen, K. et al. Urea electrosynthesis from nitrate and CO$_2$ on diatomic alloys. *Adv. Mater.* **36**, 2402160 (2024).

19. Du, W. et al. Synergistic Cu single atoms and MoS_2-edges for tandem electrocatalytic reduction of NO_3^- and CO_2 to urea. *Adv. Energy Mater.* **14**, 2401765 (2024).

20. Zhang, Y. et al. Promoting electroreduction of CO_2 and NO_3^- to urea via tandem catalysis of Zn single atoms and In_2O_{3-x}. *Adv. Energy Mater.* **14**, 2402309 (2024).

21. Zhu, R., Qin, Y., Wu, T., Ding, S. & Su, Y. Periodic defect engineering of iron–nitrogen–carbon catalysts for nitrate electroreduction to ammonia. *Small* **20**, 2307315 (2024).

22. Cheng, X. et al. Unveiling structural evolution of Fe single atom catalyst in nitrate reduction for enhanced electrocatalytic ammonia synthesis. *Nano Res.* **17**, 6826–6832 (2024).

23. Wei, T., Zhou, J. & An, X. Recent advances in single-atom catalysts (SACs) for photocatalytic applications. *Mater. Rep. Energy* **4**, 100285 (2024).

24. Huang, G. et al. Anion-regulated active nickel site for nitrate reduction in efficient ammonia electrosynthesis and Zn-Nitrate Battery. *Adv. Funct. Mater.* 2500577. https://doi.org/10.1002/adfm.202500577 (2025).

25. Lu, X., Wei, J., Lin, H., Li, Y. & Li, Y.-Y. Boron regulated Fe single-atom structures for electrocatalytic nitrate reduction to ammonia. *ACS Appl. Nano Mater.* **7**, 14654–14664 (2024).

26. Liang, C. et al. Rational regulation of Cu species in N-doped carbon-hosted Cu-based single-atom electrocatalysts for the conversion of nitrate to ammonia. *Coord. Chem. Rev.* **522**, 216174 (2025).

27. Zhang, W., Zhao, Y., Huang, W., Huang, T. & Wu, B. Coordination environment manipulation of single atom catalysts: regulation strategies, characterization techniques and applications. *Coord. Chem. Rev.* **515**, 215952 (2024).

28. Xu, Y. et al. Electronic metal–support interaction triggering interfacial charge polarization over CuPd/N-doped-C nanohybrids drives selectively electrocatalytic conversion of nitrate to ammonia. *Small* **18**, 2203335 (2022).

29. yang, Y. et al. Research progress on adsorption mechanism of radioactive iodine by metal-organic framework composites. *China Powder Technol.* **30**, 151–160 (2024).

30. Liu, C. et al. The "4 + 1" strategy fabrication of iron single-atom catalysts with selective high-valent iron-oxo species generation. *Proc. Natl. Acad. Sci. USA* **121**, e2322283121 (2024).

31. Zheng, S.-J. et al. Unveiling ionized interfacial water-induced localized H^* enrichment for electrocatalytic nitrate reduction. *Angew. Chem. Int. Ed.* **64**, e202413033 (2025).

32. Liu, L. & Corma, A. Bimetallic sites for catalysis: from binuclear metal sites to bimetallic nanoclusters and nanoparticles. *Chem. Rev.* **123**, 4855–4933 (2023).

33. Hu, Y. et al. Entropy-engineered middle-in synthesis of dual single-atom compounds for nitrate reduction reaction. *ACS Nano* **18**, 23168–23180 (2024).

34. Guo, T., Zhou, D. & Zhang, C. Perspectives on electrochemical nitrogen fixation catalyzed by two-dimensional MXenes. *Mater. Rep. Energy* **2**, 100076 (2022).

35. Jang, W. et al. Homogeneously mixed Cu–Co bimetallic catalyst derived from hydroxy double salt for industrial-level high-rate nitrate-to-ammonia electrosynthesis. *J. Am. Chem. Soc.* **146**, 27417–27428 (2024).

36. Wang, Y. et al. NH_3-induced in situ etching strategy derived 3D-interconnected porous MXene/carbon dots films for high performance flexible supercapacitors. *Nano-Micro Lett.* **15**, 231 (2023).

37. Hu, Q. et al. Subnanometric nickel phosphide heteroclusters with highly active $Ni^{\delta+}$–$P^{\delta-}$ pairs for nitrate reduction toward ammonia. *J. Am. Chem. Soc.* **147**, 12228–12238 (2025).

38. Li, Z. et al. Single-atom Co meets remote Fe for a synergistic boost in oxygen electrocatalysis. *Adv. Energy Mater.* **15**, 2500617 (2025).

39. Wang, Y. et al. Co-engineering of Fe–Mn nanoclusters with porous carbon for enhanced electrocatalytic ammonia synthesis. *Chem. Commun.* **61**, 4399–4402 (2025).

40. Ma, X. et al. S-doped mesoporous graphene modified separator for high performance lithium-sulfur batteries. *Mater. Rep. Energy* **4**, 100279 (2024).

41. Liu, Z., Ma, J., Hong, M. & Sun, R. Potassium and sulfur dual sites on highly crystalline carbon nitride for photocatalytic biorefinery and CO_2 reduction. *ACS Catal.* **13**, 2106–2117 (2023).

42. Tan, X. et al. Synthesis of NiMo–$NiMoO_x$ with crystalline/amorphous heterointerface for enhanced hydrogen evolution reaction. *Nano Res.* **18**, 94907368 (2025).

43. Peng, M. et al. Bioinspired Fe3C@C as highly efficient electrocatalyst for nitrogen reduction reaction under ambient conditions. *ACS Appl. Mater. Interfaces* **11**, 40062–40068 (2019).

44. Zhao, D. et al. Ni–Co bimetallic phosphide catalyst toward electrocatalytic ammonia synthesis under ambient conditions. *RSC Adv.* **15**, 10390–10394 (2025).

45. Wang, Y. et al. Interfacial water structure modulation on unconventional phase non-precious metal alloy nanostructures for efficient nitrate electroreduction to ammonia in neutral media. *Angew. Chem. Int. Ed.* **64**, e202508617 (2025).

46. Wang, X. et al. Harnessing Spin-Lattice Interplay in Metal Nitrides for Efficient Ammonia Electrosynthesis. *Adv. Mater.* 2504505. https://doi.org/10.1002/adma.202504505 (2025).

47. Liu, W. et al. Regulating local electron distribution of Cu electrocatalyst via boron doping for boosting rapid absorption and conversion of nitrate to ammonia. *Adv. Funct. Mater.* **34**, 2408732 (2024).

48. Rao, X. et al. A porous Co_3O_4-carbon paper electrode enabling nearly 100% electrocatalytic reduction of nitrate to ammonia. *Mater. Rep. Energy* **3**, 100216 (2023).

49. Wang, Z. et al. Synergy of single atoms and sulfur vacancies for advanced polysulfide–iodide redox flow battery. *Nat. Commun.* **16**, 2885 (2025).

50. Ye, W. et al. Continuous intermediates spillover boosts electrochemical nitrate conversion to ammonia over dual single-atom alloy. *Angew. Chem. Int. Ed.* e202509303. https://doi.org/10.1002/anie.202509303 (2025).

51. Wang, G. et al. NiMoO4 nanorods with oxygen vacancies self-supported on Ni foam towards high-efficiency electrocatalytic conversion of nitrite to ammonia. *J. Colloid Interface Sci.* **647**, 73–80 (2023).

52. Ge, J. et al. Al-Ce intermetallic phase for ambient high-performance electrocatalytic reduction of nitrate to ammonia. *ChemCatChem* **15**, e202300795 (2023).

53. Yang, M. et al. NiMo-based alloy and its sulfides for energy-saving hydrogen production via sulfion oxidation assisted alkaline seawater splitting. *Chin. Chem. Lett.* **36**, 110861 (2025).

54. Luo, J. et al. Local microenvironment reactive zone engineering promotes water activation. *Mater. Rep. Energy* **5**, 100327 (2025).

55. Li, X. & Hu, W. Review of design strategies for particle catalysts used in electrocatalytic CO_2 reduction in acidic media. *China Powder Sci. Technol.* **31**, 81–90 (2025).

56. Lu, Y., Liu, W. & Jiang, Y. Research progress on oxidase-like performance of cobalt-based single-atom catalysts. *China Powder Sci. Technol.* **31**, 66–74 (2025).

57. Wang, W., Chen, J. & Tse, E. C. M. Synergy between Cu and Co in a layered double hydroxide enables close to 100% nitrate-to-ammonia selectivity. *J. Am. Chem. Soc.* **145**, 26678–26687 (2023).

Acknowledgements

Author contributions

M. Yang and M. Chen synthesized, characterized and performed electrochemical tests, to which J. Ma contributed. L. Zhang performed the in-situ FTIR calculations, to which Y. Feng and L. Zhuo contributed. Y. Wang, C. Hu and X. Liu co-edited the paper. M. Yang and M. Chen co-wrote the paper. X. Liu supervised this work.

Competing interests

The authors declare no competing interests.

Additional information